The Characteristics of Cloud Macro Parameters Caused by Seeder-Feeder Process inside Clouds Measured by Millimeter-wave Cloud Radar in Xi'an， China

Huige Di*, Yun Yuan

School of Mechanical and Precision Instrument Engineering, Xi'an University of Technology, Xi'an 710048, China

* Corresponding author: dihuige@xaut.edu.cn

Abstract

The seeding effect of upper clouds on lower clouds affects the evolution of clouds, especially the seeding from upper ice clouds on lower stratiform clouds or convective clouds, which can stimulate the precipitation of lower clouds and even produce extreme precipitation. Because when seeders of seeding cloud enter the feeding cloud, the interaction between cloud particles results in the change of macro and micro parameters of the feeding cloud. Based on the observation data of the ground-based Ka-band millimeter-wave cloud radar (MMCR) and microwave radiometer (MWR) in spring and autumn from 2021 to 2022, the seeder-feeder phenomenon among double-layer clouds in Xi'an, China, was studied. The study on 11cases of seeder-feeder processes shows that the processes can be divided into three categories by defining the height difference (HD) between the seeding cloud base and the feeding cloud top, and the effective seeding depth (ESD). Through the analysis on the reflectivity factor and the radial velocity of cloud particles detected by MMCR and on the retrieved cloud dynamics parameters (vertical velocity of airflow and terminal velocity of cloud particles), it is shown that the reflectivity factor in the cloud is significantly enhanced during the seeder-feeder period for the three types of processes. But the magnitudes of the enhancements among the three seeder-feeder processes are different. The results also showed the limited depth as seeders entering the top of the feeding cloud. The lower the height and thinner the thickness of the HD, the lower the height and thicker the thickness of ESD; On the contrary, the higher the height and the thicker the thickness of the HD, the higher the height and the thinner the thickness of the ESD.

Keywords: Macro parameters of cloud; Natural seeder-feeder process; Ka-band millimeter-wave cloud radar; Remote sensing and sensors

1．Introduction

Natural ice crystals in upper clouds can be a source of seeders for lower clouds (Korolev et al., 1999; Heymsfield et al., 2013; Myagkov et al., 2016; Cheng et al., 2020; Wang et al., 2023). This seeder-feeder process is able to promote the development of the lower clouds even to stimulate extreme precipitation (Choularton et al., 1986; Locatelliet al., 1983; Robichaud al., 1988; Fernández-González et al., 2015; Ramelli et al., 2021). The seeder-feeder phenomenon shows that ice crystals as seeder, from an upper cloud fall into a lower cloud or a lower-lying part of the same cloud， which is either liquid phase, ice or mixed phase (Hall et al., 1976; Korolev et al., 2003; Hong et al., 2005; Geerts et al., 2015; Lowenthal et al., 2018). When ice crystals meet lower cloud droplets with ice phase or in supercool water state, they grow by riming or vapor deposition via the Wegener-Bergeron-Findeisen effect (Bergeron 1935; He et al., 2022). Therefore, it is important to understand the seeder-feeder mechanism, which can be helpful to improve the representation of cloud processes in weather and climate models, and weather forecasts of precipitation, and ultimately to reduce uncertainty in climate simulations (Hong et al., 2012; Proske et al., 2021). The seeder-feeder phenomenon has been studied by observations and simulations in operations of the artificial precipitation enhancement, and it was found that the distinct changes in both cloud and precipitation properties (French et al., 2018; Ramelli et al., 2021; Dong et al., 2021).

Historically, Braham (1967) noted the natural phenomenon of ice crystals from the upper cirrus clouds acting as seeders for ice formation in warmer clouds below. It was found that not only cirrus but also altocumulus and altostratus, which contain ice crystals, may act as the seeding clouds. In the 1980s in China, Hong et al., (2012) established a cloud model that simulated the formation of stratiform clouds. In the model, the seeder-feeder process was emphasized. Subsequently, this cloud seeding process through sedimenting ice crystals has been observed in a multitude of remote sensing and aircraft campaigns. Seifert et al., (2014) and He et al., (2022) estimated the occurrence frequency of the natural cloud seeding through analyzing their lidar datasets. Furthermore, a regional occurrence frequency of seeder-feeder in the Arctic was estimated by Vassel et al. (2019). They pointed out that the seeder-feeder process happened usually within multi-layer clouds, which was observed by radiosonde and radar in Svalbard. By using the DARDAR satellite products and sublimation calculations, Proske et al., (2021) also studied the occurrence frequency of cloud seeding in Switzerland and found the high occurrence frequency of seeding situations with the survival of the ice crystals. The microphysical parameters of the seeder-feeder process appeared within mixed-phase clouds have been investigated by using the ground-based remote sensing instruments (Ramelli et al., 2021). However, there is still a lack of the specific characteristics, such as the height difference between the seeding cloud base and the feeding cloud top (HD) and the effective seeding depth (ESD), to represent the feature of the seeder-feeder process. In the meantime, the characteristic of air vertical motion, particle terminal velocity inside cloud during seeder-feeder process is still poorly understood.

Actually, the seeder-feeder process within clouds is not well documented in the literature (Hill et al., 2007; Purdy et al., 2005; He et al., 2022). The main reason is that the effects of the seeder-feeder process are not easy to be measured, because several cloud layers need to be able to monitor simultaneously with high vertical and temporal resolution. The active instrument of the Ka-band millimeter-wave cloud radar (MMCR), a useful tool for cloud observations, is capable of detecting multiple cloud layers directly, which allows measure the seeder-feeder process (Ramelli et al., 2021; Proske et al., 2021). The Doppler spectra (*SP*) generated by MMCR can be used to retrieve vertical velocity of airflow and the terminal velocity of cloud particles and to obtain information of particle types (Luke et al., 2013; Shupe et al., 2008; Kollias et al., 2002 and 2011). However, such direct observations of ice crystal formation and evolution in the seeder-feeder process are limited (French et al., 2018).

In this study, the seeder-feeder phenomenon happened between bilayer stratiform cloud in Xi'an were studied by using observation data from the MMCR together with microwave radiometer (MWR) and radiosonde measurements from January 2021 to December 2022. In this paper, following the above review of study status on the seeder-feeder process, the used instruments and methods associated with datasets are introduced simply, then through a case analysis of seeder-feeder process measured by MMCR to expose the evolution mechanism of seeding cloud and feeding cloud. The main results and conclusions will be represented by statistics with two years data.

2. Instruments and methods

The instruments used in this study are MMCR, MWR, radiosonde and Raindrop Spectrometer (RDS). The MMCR is the Doppler vertical pointing cloud profile radar with solid-state transmitter. The main parameters of the MMCR are shown in Table 1. The MMCR can observe reflectivity factor (Z), radial velocity (V_r), *SP* and spectral width (σ). These parameters can be used to retrieve cloud dynamic parameters, such as cloud particle terminal velocity and vertical velocity of airflow inside the cloud (Liu et al., 2019; Yuan et al., 2022; Di et al., 2022). Because of the advantages of solid-state transmitter, the MMCR is small in size, long in life and good in reliability, so it provides reliable observation data for this study. Due to the MMCR has certain penetrating ability to cloud, it can detect the structure variation of multi-layer cloud system, so the seeder-feeder phenomenon between multi-layer cloud system can be measured, which is an important reason for us to choose this instrument in this study.

The MWR includes 21 water vapor channels (distributed in K band, that is, 22–31 GHz), 14 air temperature channels (distributed in V band, that is, 51~59 GHz), and 1 infrared channel. The observation data of MWR can be used to retrieve the profiles of atmospheric temperature (/K) and relative humidity (/%), integrated water vapor content (Vint /mm) and integrated liquid water content (Lqint /mm). Below the height of 2 km, the root mean square error (RMSE) of temperature measurement is less than 1 K, the RMSE of temperature measurement is less than 1.8 K above 2 km height. The RMSE of relative humidity is less than 15 %, and the RMSE of Vint is less than 4 mm. The relevant parameters of MWR are shown in Table 2.

Table 1 Major technical parameters of the MMCR

Order	Items	Technical specifications
1	Radar system	Coherent, pulsed Doppler; solid-state transmitter; and pulse compression
2	Radar frequency	35 GHz ± 200 MHz (Ka-band)
3	Antenna aperture	≥1.6 m
4	Horizontal and vertical beam width	0.4°and 0.4° beam width
5	Antenna gain	53 dB
6	Pulse repeat frequency	8000 Hz
7	Peak power	≥20 W
8	Detecting parameters Detection capability	*Z*, *Vr*, *σ*, and *SP* ≤ −35 dBz at 5 km
9	Range of detection	Height: 0.15 – 15 km Reflectivity: −45 – + 30 dBz Radial velocity: −15 – 15 ms^{-1} Spectrum width: 0–15 ms^{-1}
10	Spatial and temporal resolutions	Temporal resolution: 5 s Height resolution: 30 m
11	Pulse width	1 µs; 5 µs; and 20 µs

Table 2 Major technical parameters of MWR

Order	Items	Technical specifications
1	Range of detection	0 – 10 km
2	Height resolution	≤ 25 m (0~ – 500 m) ≤ 50 m (500 – 2000 m) ≤ 250 m (2 – 10 km)
3	Layering	≥83 layers
4	Channel frequency	K-band: 22 – 31 GHz V-band: 51 – 59 GHz
5	Number of channels	number of water vapor channel: 12 number of temperature channel: 14 number of infrared channel: 1
6	Absolute brightness temperature accuracy	≤1.0 K
7	RMSE of temperature profile	≤ 1.8 K， Range >2 km ≤ 1.0 K， Range ≤2 km
8	RMSE of relative humidity	≤15%
9	RMSE of Vint	≤4 mm

The above instruments were placed at the Jinghe National Meteorological Station (108°58'E, 34°26'N, as shown in Fig. 1) in Xi'an, Shaanxi Province, China, which is located near the north bank of the Wei River in Guanzhong Basin (between 107°40'–109°49'E, 33°42'–34°45'N, about 400 meters above sea level) in the middle of the Yellow River Basin. The Qinling Mountains on the south side of the Wei River often block the cold air southward in winter and spring, and produce stable stratiform clouds in the Guanzhong Plain, which provides a natural experimental site to study the phenomenon and mechanism of seeder-feeder of bilayer stratiform clouds. The distance between MMCR and MWR is less than 5m, and the distance between other instruments is less than 50 m. The Jinghe National Meteorological Station is also the national Meteorological sounding Station. Sounding balloons are released every day at 07:15 and 19:15 BJT (Beijing Time) to detect atmospheric temperature, humidity, wind speed and direction from the ground to an altitude of 30 km above the station (Görsdorf et al., 2015; Vassel et al. 2019；Yuan et al. 2022). The collaborative detection of the above instruments provides effective data support for capturing the seeder-feeder process in clouds in this study.

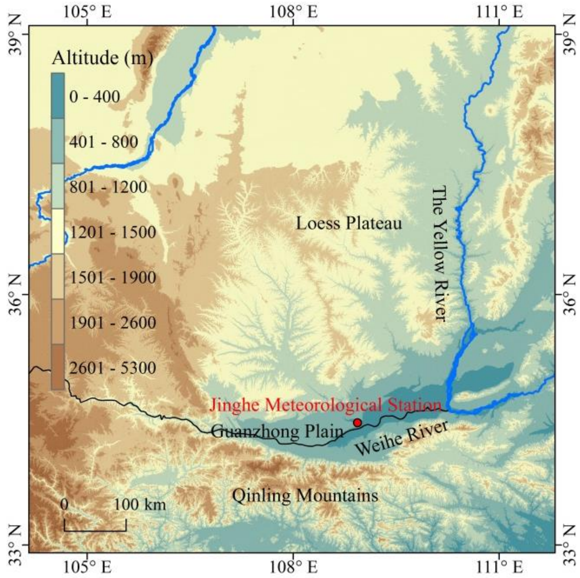

Figure 1 Geographical coverage around observation site (104°10'~111°40'E, 33°-39°N). The red dot indicates the location of the Jinghe National Meteorological Station in Xi'an (107°40'-109°49'E, 33°42'-34°45'N).

As the MMCR adopts vertical upward mode observation, its echo signal will not be affected by ground clutter, which reduces errors of the terrain clutter in observation data. However, due to the influence of aerosol and insects in lower atmosphere, there will be non-cloud signals in the bottom echo signal of the MMCR. The non-cloud echo signals in the low-level atmosphere have the characteristics of the small reflectivity factor, low velocity, and large spectral width. To further eliminate interfering wave information, we obtained the data quality control threshold by counting the characteristic changes in planktonic echoes in the boundary layer under cloud free conditions (Yuan et al., 2022). The *SP* measured by MMCR includes the information of the cloud particle size and the air vertical motion. The *SP* is also affected by radar beam width, ambient wind shear and atmospheric turbulence. Therefore, radiosonde data combined with the MMCR hardware parameters were used to correct the broadening of *SP*, in order to improve the accuracy of the retrieved vertical velocity of airflow and the particles terminal velocity in clouds (Doviak and Zrnic, 1993; Shupe et al., 2008; Kollias et al., 2001 and 2002; Shupe et al., 2008 and 2004).

To calculate the vertical velocity of the airflow in the cloud more accurately, the cloud phase state was judged. The terminal velocity of cloud particles varies due to the influence of phase state, which in turn affects the magnitude of vertical airflow velocity. Cloud particle phase identification adopts cluster analysis method (Shupe, 2007). The specific process takes cloud reflectivity factor, particle radial velocity and spectrum width measured by the MMCR, and atmospheric temperature measured by MWR as input parameters for cloud phase identification. Through unsupervised learning, cloud particles of different phase states in the cloud were identified, such as warm clouds, mixed phase (ice dominated phase or water dominated phase), ice, snow, supercooled water, drizzle, rain and graupel particles. In the identified ice particle region and mixed phase region, the small particle tracer method was used to obtain the vertical velocity of the airflow (Shupe et al., 2008).

In the identified supercooled water region, the peak position of the liquid cloud particle is used to obtain the vertical velocity of airflow (Wei et al., 2019). When it drizzles, the *SP* of MMCR usually shows the bimodal distribution, and the vertical velocity of the airflow in the cloud can be obtained by the bimodal position of the liquid cloud particles (Wei et al., 2019; Luke et al., 2010 and 2013). The terminal velocity of cloud particles and the vertical velocity of airflow are important parameters in the seeder-feeder process. Based on the observation data of MMCR from 2021 to 2022 (a total of 10363 hours), the seeder-feeder phenomenon of bilayer cloud system (ice phase in upper cloud and mixed phase cloud in lower cloud) will be analyzed below.

3. Parameter Definition and Case Analysis

To conveniently and clearly analyze the seeder-feeder process of bilayer clouds in Xi 'an, and find how the upper seeding clouds to seed the lower feeding clouds in this study. We have chosen observation data of MMCR and MWR in winter and spring, as most of the clouds in these seasons are stable stratiform clouds. The first step is to define the relevant parameters to describe the characteristics of the bilayer clouds, such as the top height of seeding cloud (THSC) and the base height of seeding cloud (BHSC), the top height of feeding cloud (THFC). The height difference (HD) between BHSC and THFC is also defined. The HD can display directly one of the geometric features of the bilayer clouds. The heights of cloud top and bottom are determined from radar echo signals. Before determining the two heights, the clutter mixed in signals observed by MWCR were filtered out. The sensitivity threshold of the radar used in this study is -40dBz, which is sufficient for accurately observing the positions of cloud base and cloud top (Yuan, et al. 2022).

A period of stable time before the seeding cloud began to seed was denoted as t1, the moment when the seeding cloud began to seed was marked as T0, the length of time period of the seeding was denoted as t2, and the period after the end of the seeding but the lower part of the feeding cloud still showed development changes in reflectivity factor was labeled as t3 (which is called the duration of the seeding effect). Usually, the cloud base or cloud top is not flat enough. However, as our study focuses on stable stratiform clouds, the cloud tops and cloud bases observed in these cases are relatively flat. THSC is the average height of seed cloud tops during the observation period, BHSC is the average value of the seeder cloud base during the t1 period, and THFC is the average value of the feeder cloud top during the t1 period.

Fig. 2 shows the cloud reflectivity factor and radial velocity detected by MMCR from 23:00 BJT on 05 February, 2022 to 04:00 BJT on 05 February, 2022. The reflectivity factor (Fig. 2a) clearly shows the seeder-feeder process. The period from 00:40 to 02:20 BJT, cloud particles of the upper cloud fall into the top of the lower cloud. This is confirmed by the cloud particle radial velocity (Fig. 2b), which shows that the cloud particles during the period are all sinking, and the sinking velocity is about -1ms^{-1}. The above defined parameters have been marked in Fig. 2a. It also shown that the bilayer cloud is stable during this period, with THSC at 8 km, BHSC at 5.5 km, THFC at 4.2 km, HD at 0.85 km. The seeding process lasts for about 98.2 minutes (t2), and feeding cloud development duration reaches more than 2 hours and 30 minutes. Before seeder-feeder process of the bilayer clouds, only 40 minutes (t1) is considered as the earlier state of beclouds, as detailed in Table 3.

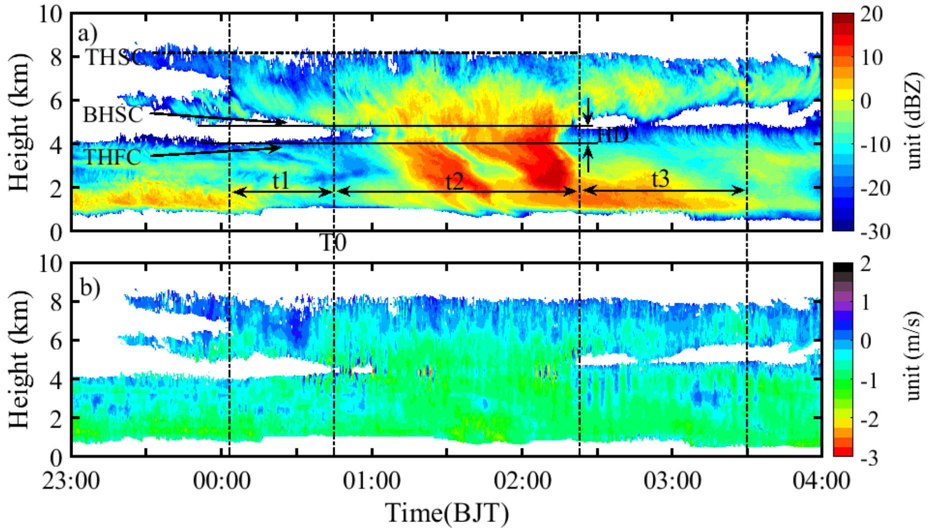

Figure 2 The variations with time for both profiles of cloud reflectivity factor (a) and cloud particle radial velocity (b) detected by MMCR from 23:00 BJT on 05 February, 2022 to 04:00 BJT on 06 February, 2022 (positive value in color bar represents ascending motion and negative value represents sinking motion). In the figure, THSC and BHSC are the cloud top height and cloud base height of the seeding cloud, THFC is the cloud top height of the feeding cloud, and HD is the height difference between the base height of seeding cloud and the top height of feeding cloud. T0 is the moment when the seeding cloud began to seed, t1 is the stable time period before the seeding cloud begins to seed, t2 is the length of time from the beginning to the end of the seeding, and t3 is the period after the end of the seeding but the reflectivity factor in the feeding cloud still development.

Table 3 Values of the defined parameters for the seeder-feeder phenomenon observed by MMCR from 23:00 BJT on 05 February, 2022 to 04:00 BJT on 06 February, 2022.

Parameters	THSC /(km)	BHSC /(km)	THFC /(km)	HD /(km)	t1 /(min)	t2 /(min)	t3 /(min)
Values	8.2	5.1	4.3	0.85	40.2	98.2	44

In order to reveal the variation characteristics of the cloud system during this seeder-feeder process, the spectrum width of cloud particles, vertical velocity of the airflow, and the terminal velocity of cloud particles were firstly calculated from the signals of the *SP* detected by MMCR (as shown in Fig. 3, the positive value of the velocity is specified as the ascending motion and the negative value is the descending motion). Fig. 3a shows that the spectrum width is small, indicating that the cloud particle radial velocity detected by MMCR is relatively stable, which also indicates that the airflow inside bilayer clouds is stable. The maximum velocity spectrum width is about 0.6 ms^{-1}, which is mainly located at the top of the seeding and feeding clouds (especially at the beginning of the feeding cloud), and the lower part between the seeding and the feeding cloud during the seeding period (that is, the top of the feeding cloud). In addition, the feeding cloud showed changes in the t3 period after seeding, that is, the feeding cloud top height rose slightly (Fig. 2a), and the spectrum width increased at the cloud top zone, which says that the radial velocity at this zone changed greatly during the t3 period. This is probably because of latent heating release by the phase transition in the seeding cloud during seeder-feeder process, which will be feedback the dynamic process, then increases the vertical velocity of the airflow inside the cloud. This position in Fig. 3b indeed indicates that the vertical velocity of the airflow is relatively large (0.5–2 ms^{-1}). Fig. 3b shows that weak upward movement (0.5–2 ms^{-1}) prevails in the seeding clouds and the feeding clouds, which is consistent with the dynamic structure characteristics of stable stratiform clouds (Hou et al., 2010; Wang et al., 2022) in winter and spring in Xi'an region. The maximum vertical velocity of airflow was located at the junction of upper and lower clouds, the top and base of seeding clouds and the top of feeding clouds in t3 period. During the seeding period, there are the large airflow upward movement (up to 1.5 ms^{-1}) in the middle and lower zones of the feeding cloud. There is rarely a large-scale and prolonged air sinking and rising movement in the seeding cloud and feeding cloud, but alternating upward and downward movements occur.

Fig. 3c clearly shows the terminal velocity of cloud particles, and it is in the range of –1~ –4 ms^{-1} during seeding process, but most of them are less than -2.5 m/s. During this seeding process, 00:45–01:50 BJT and 02:00–02:20 BJT are two significant seeding periods, and the maximum terminal velocity of cloud particles is about –4 ms^{-1} in last period, which indicates the large cloud particles size. According to the cloud phase in Fig. 4, the particles are snowflakes in the cloud seeding and feeding area. The particle size is related to the shape of snowflakes and the terminal velocity, so it difficult to accurately quantify particle size. The relations of snow particles and diameter are studied in the ref. (Tao et al. 2020). According to the speculation, the size of the snow particles in the cloud is distributed between 1mm and 6mm, and most of them are below 3mm. In the areas unaffected by seeding (except for the bottom area of the lower cloud during the time period of 23:00-24:10), the particle terminal velocity is small, less than -1.5ms^{-1}. These all indicates that seeding has a significant enhancing effect on particle size of feeding clouds.

According to Table 2, the height difference (HD) between seeding and feeding cloud is 0.85 km. If the sinking speed of cloud particles is at –1 ms^{-1} (Fig. 2b), it takes about 14 minutes for cloud particles to fall from the seeding cloud base to the feeding cloud top. In addition, Fig. 2 and Fig.3 show that seeding end at 02:20 BJT, but Fig. 2b still shows that after this time, cloud particles still sink (at 02:45 BJT, sinking velocity <–0.5 ms^{-1}) on the feeding cloud top. It is likely that MMCR is limited in its sensitivity to detect smaller particles and cannot clearly show the reflectively factor of small particles. The above results indicate that the sinking motion region (time period) of the cloud particle velocity can be used to identify the seeding cloud effectively. Anyway, the above gives an important conclusion, i.e. after seeding, the feeding cloud top rose slightly, which may be the result of latent heating release. The sinking motion zone of particle velocity can directly characterize the seeding process.

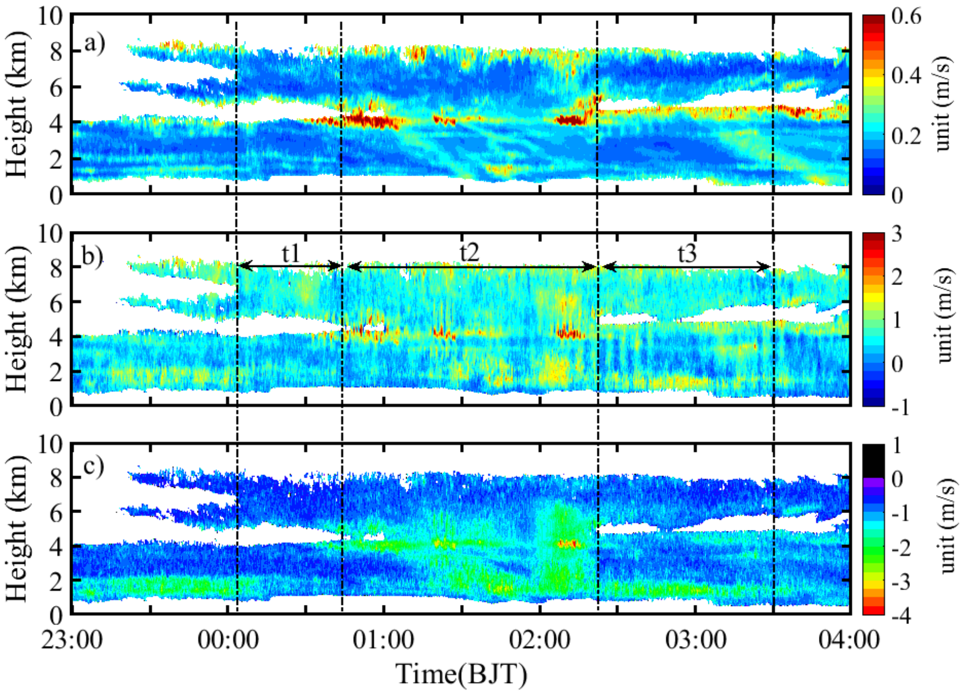

Figure 3 The spectrum width of cloud particles (a), vertical velocity of the airflow (b), and the terminal velocity of cloud particles (c) based on the retrieval from MMCR (positive value in the color bar represents ascending motion and negative value represents sinking motion) .

By using the data of MMCR and MWR observations, the phase state and water vapor structure of the cloud, the total amount of liquid water and water vapor in the column can be retrieved. Fig. 4a shows that seeding clouds consist of ice and snow, and seeding is caused by sinking ice particles. Before seeding, the particles in the feeding cloud were basically in mixed phase, and there was a thin layer of supercooled water in the middle and upper part of the cloud, and snow particles appeared at the base of the cloud for a short time after 00:10 BJT. Before seeding, the larger downward mean Doppler velocity (Figure 2b) was detected in the lower part of the seeding cloud, which indicates that the cloud process has transformed from ice to snow with large particle sizes. Snowflakes, as seeders, fall into the mixed phase cloud containing supercooled water, so that the Wegener-Bergeron-Findeisen effect occurred. That effect causes the supercooled water in the mixed phase cloud to rapidly transform into ice. Because it takes time for particles to fall, so the seeding will continue to the middle and lower parts of the feeding clouds, and snow keeps for a long time (maintaining the entire t3 period); In the top region of the unaffected feeding cloud, the cloud phase remains supercooled water, which is consistent with the observation results in Shupe (2007). The temperature of the supercooled water layer is close to –20°C, while that of the seeding cloud top is close to –40°C. From Figure 4, it can be seen that the instantaneous water vapor flux of the seeding cloud is smaller than that of the feeding cloud, and the bottom layer of the feeding cloud has the instantaneous water vapor flux greater than 20 $gm^{-2}s^{-1}$, indicating that the lower layer of the atmosphere has high humidity during the seeder-feeder process in bilayer stratiform cloud.

The temporal variation of column water vapor and column liquid water given by MWR (Fig. 4c) showed that both rapidly increased from t1 before seeding to the beginning of seeding, and rapidly decreased after seeding. Before the second intense seeding, column water vapor and column liquid water content increased rapidly, and then decreased with the end of seeding. This process can be understood as that when the ice phase particles of the seeding cloud enter the supercooled water of the feeding cloud top, the Wegener-Bergeron-Findeisen effect is triggered, and the liquid particles are rapidly transformed into ice phase particles, which leads to the reduction of liquid water content in the column. Therefore, the Wegener-Bergeron-Findeisen effect is the main reason for the reduction of liquid water content in the column. The above results illustrate that the seeders of seeding cloud cause the change of cloud phase state in the feeding cloud, thus reducing the water vapor and liquid water in the column. The rapid increase of water vapor and liquid water in the column before seeding may be related to the change of atmospheric environment at that time, which still needs to be studied in detail.

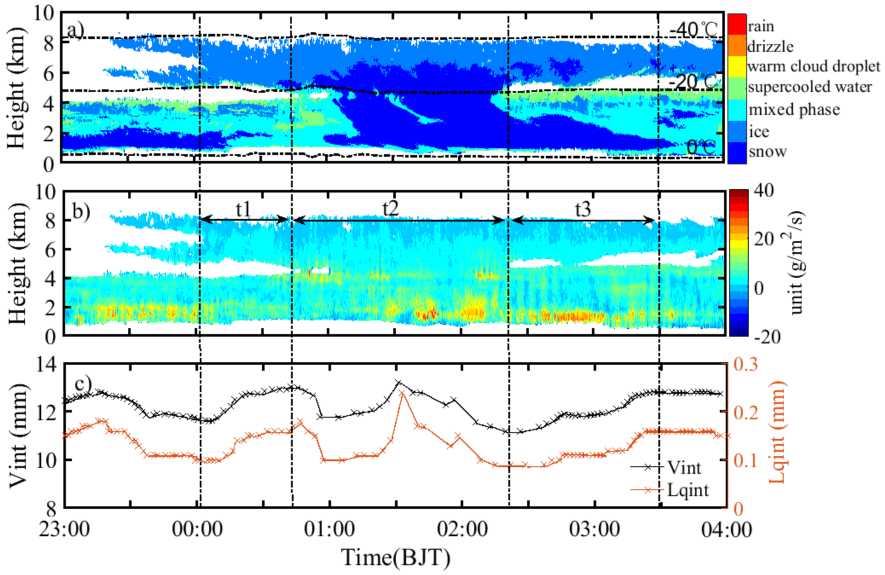

Figure 4 The variations of cloud phase (a), water vapor flux (b), integrated water vapor content (Vint: black line) and integrated liquid water content (Lqint: Orange line) (c) with time observed and retrieved by MMCR and MWR.

According to the radar formula, the echo signal intensity is proportional to the sixth square of the cloud particle diameter. The cloud particle with larger diameter has a larger falling speed under the action of gravity. In order to reveal the relationship between particle size and echo signal in the seeder-feeder process. The statistical classification method of equal samples is adopted to find the relationship. All signal values (echo reflectivity, radial velocity, spectral width, particle falling velocity, and vertical airflow velocity) are reordered according to their corresponding echo reflectivity values from small to large, and then compared in the equal sample. For example, the first 33%, middle 33% and last 33% of the sample are arithmetically averaged to obtain the mean reflecting the weak, moderate and strong values respectively. This has the advantage of avoiding the defect of large and small arithmetic averages cancelling each other out. Following this principle, the reflectivity factors of t1, t2 and t3 are arranged in ascending order, and the corresponding parameters of cloud particles are also sorted with the order of reflectivity factors, and then the arithmetic average is performed according to the first 33%, middle 33% and last 33% of the sample. The average profile representing weak echo, moderate echo and strong echo (as shown in Figs 5a1, a2, a3) is obtained, and the corresponding average profile of cloud particle parameter for the three intensity echoes is also obtained, and they are the corresponding average profiles of cloud particle radial velocity (Figs 5b1, b2, b3), average profiles of velocity spectrum width (Figs 5c1, c2, c3), average profiles of particle terminal velocity (Figs 5d1, d2,d3) and average profiles of vertical velocity of the airflow (Figs 5e1, e2, e3).

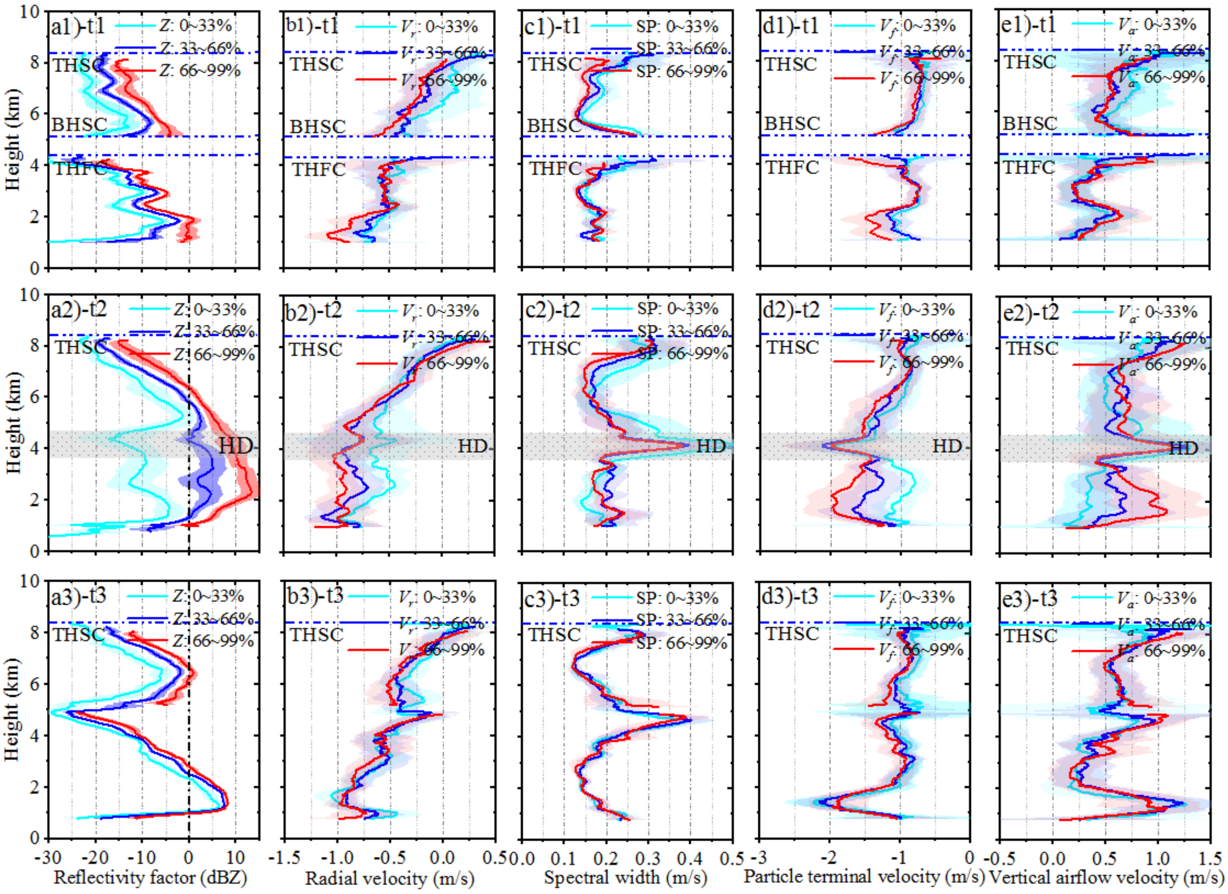

Figure 5 The mean profiles of reflectivity factor (a1, a2, a3), radial velocity (b1, b2, b3), spectrum width (c1, c2, c3), particle terminal velocity (d1, d2, d3) and vertical velocity of the airflow (e1, e2, e3) during t1 (up), t2 (middle) and t3 (bottom) periods, respectively. In the figure, the cyan line, blue line and red line represent the average of the first 33%, the middle 33% and the last 33% of the sample respectively; the solid line represents the mean, and the shaded area of the corresponding color is the variance.

The up panel of Fig. 5 shows that there are obvious differences (a1) between the weak, moderate and strong reflectivity factor profiles of seeding clouds and feeding clouds before seeding (t1 period), but in general, the average profiles of the three kinds of echo intensity show that reflectivity factor increases with the decrease of height, and the values of the profiles are relatively small (all less than 0 dBZ) and the variance is also small. However, the profiles of cloud particle radial velocity (b1), spectral width (c1), particle terminal velocity (d1) and vertical velocity of the airflow (e1) corresponding to the average profiles of the three intensity reflectivity factors basically coincide, and do not show significant changes in these parameters caused by differences in reflectivity factors. This indicates that the cloud particle states (radial velocity, spectrum width, particle terminal velocity and vertical velocity of airflow) of seeding and feeding clouds in t1 period are uniformly distributed at different intensity echoes, that is, the upper and lower cloud systems are stable before seeding, and the size of cloud particles is mainly small.

The middle panel of Fig. 5 represents the average profiles of each parameter during the seeding period (t2). Fig. 5 a2 shows that the difference between the average profiles of the reflectivity factors for the three kinds of echo intensity is greater than that before seeding. In particular, the profiles of the moderate and strong reflectivity factors in the figure increases significantly, reaching a maximum of 15 dBZ, which hints that the size distribution of cloud particles in the bilayer cloud varies significantly during seeding. Compared with before seeding, the reflectivity factor of the lower part of the seeding cloud (5.4 km ~ 6.2 km) increased significantly, and the radial velocity of cloud particles (Fig. 5 b2), the terminal velocity of cloud particles (Fig. 5 d2) and the vertical velocity of airflow (Fig. 5 e2) all increased correspondingly. It was these changes of cloud particles under the seeding cloud that produced the seeding effect. The spectral width of feeding cloud particle velocity (Fig. 5 c2) corresponding to the three intensity reflectivity factors don't coincide, which significant changes in particle distribution or types across different scale ranges. For the strong reflectivity factor profile, from the top of the seeding cloud to the lower part of the feeding cloud at a height of 2 km, reflectivity factor increases rapidly with the decrease of the height, and the corresponding radial velocity and terminal velocity of the cloud particles increase (i.e. the descending velocity increases), and the vertical velocity of the airflow also increases, indicating that the large particles in the seeding cloud have a great effect on the feeding cloud. For the weak reflectivity factor profile of bilayer cloud, the average reflectivity factor changes little compared with that before seeding, indicating that the seeding effect of small cloud droplets corresponding to such weak echoes is small. Fig. 5 also shows that during the seeding period, the reflectivity factor of the middle and upper part of the feeding cloud increases significantly after the seeders are injected into the feeding cloud, especially in the case of strong and moderate intensity, indicating that the middle and upper part of the feeding cloud particles become significantly larger, which clearly expresses the seeding effect.

With the end of seeding (bottom panel in Fig. 5), the reflectivity factor of the upper and middle part of the seeding cloud decreased significantly. The reflectivity factor of the lower part of the feeding cloud increased, which reveals that the seeding effect developed to the lower part of the feeding cloud. In general, the distribution of strong, moderate and weak reflectivity factor profiles in feeding clouds was concentrated after seeding, informing that cloud particle size became more uniform, which was obviously different from that before and during seeding. Therefore, the profiles of cloud particle radial velocity, velocity spectral width, particle terminal velocity and vertical velocity of the airflow corresponding to the strong, moderate and weak reflectivity factors basically coincide. Due to the fact that echo reflectivity factor, radial velocity, and falling terminal velocity reflect particle size, and spectral width reflects particle size distribution and particle category. In the end of seeding, the cloud particle size distribution and particle velocity of the bilayer cloud may reach a relatively balanced and stable state through the complex microphysical and dynamic interactions in the t2 period. However, the reflectivity factor of the feeding cloud during t3 period reaches the maximum in the lower layer (1 km~2 km), and the corresponding radial velocity and terminal velocity of cloud particles also reach the maximum, indicating that seeding effect continues at the lower part of the feeding cloud although seeding has ended at the top of the feeding cloud. The key takeaway from Fig. 5 is that the reflectivity factor (related to cloud particle scale) and the descending velocity of cloud particles increased within a certain depth of the feeding cloud during the seeding period. After the end of seeding, there was a seeding continuation period in the middle and lower part of the feeding cloud.

In order to understand the effect of seeding cloud on feeding cloud, the correlation coefficient between cloud particle terminal velocity and reflectivity factor is calculated statistically. Firstly, the correlation coefficient between the terminal velocity of cloud particles during the seeding period (t2) and the corresponding reflectivity factor (called the autocorrelation coefficient, because the terminal velocity of cloud particles has a certain relationship with the size of cloud particles, while the reflectivity factor is proportional to the 6th power of the particle diameter) was calculated. Therefore, the cloud particle terminal velocity is not independent of the reflectivity factor. The obtained autocorrelation coefficient profile is shown in Figure 6a, which indicates that as the height decreases from the middle of the seeding cloud (6 km) to the middle and lower part of the feeding cloud (2.5 km), the autocorrelation coefficient increases from 0 to 0.8, that is, the positive correlation between the cloud particle terminal velocity and the reflectivity factor increases continuously. The reflectivity factor also increases with the decrease of altitude (from –5 dBZ to 5 dBZ), illustrating the reflectivity factor and terminal velocity of cloud particles increase with the decrease of height, which may be inferred that the size of cloud particles also increases with the decrease of height. It can be seen that during the seeding period (t2), the reflectivity factor of the middle and upper part of the feeding cloud will be large and the particle terminal velocity will increase. Therefore, the Effective Seeding Depth (ESD) is defined as the height difference between the top height of the feeding cloud and from the height down to the height of the maximum correlation coefficient, which represents the influence of seeders on the feeding cloud during t2 period. In this case, the ESD is about 1.6 km. In the ESD region, the echo intensity increases with the decrease of the height, so the cloud particle size also increases rapidly with the decrease of the height, as the result the middle and lower part of ESD is the area where the seeding effect is most intense. In the upper part of ESD (i.e. the top of the feeding cloud), the reflectivity factor is slightly smaller (less than 3 dBZ) and the correlation coefficient is also smaller (less than 0.2), indicating that the upper cloud particle size of the feeding cloud is small, and the correlation between the terminal velocity of the cloud particle and the reflectivity factor is poor, because the seeders has just entered the top of the feeding cloud and the seeding effect has just begun.

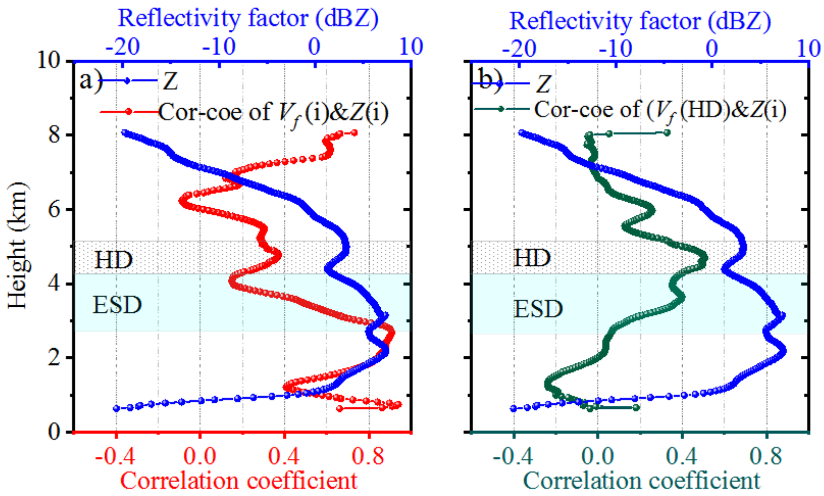

Figure 6. The autocorrelation coefficient profile (a) between cloud particle terminal velocity and reflectivity factor at each layer from top to bottom in the bilayer cloud in t2 period, and the correlation coefficient profile (b) between the average descent velocity of cloud particle in the HD region and reflectivity factor at different height layers in t2 period.

If the region between the upper and lower clouds, i.e. HD region, is regarded as a whole layer, the correlation coefficient between the average terminal velocity of cloud particles in this layer and the reflectivity factors of cloud layers during the seeding period (t2 period) (called non-autocorrelation coefficient, because the terminal velocity of cloud particles and the reflectivity factors in the non-HD region are relatively independent at this time) is calculated, and the non-autocorrelation coefficient profile in Fig. 6b is obtained. It shows that above the height of the HD region, the positive correlation between the average terminal velocity of cloud particles and the reflectivity factor of each layer of the seeding cloud increases as the height decreases, indicating that the terminal velocity of cloud particles in the HD region is mainly affected by the reflectivity factor of the lower layer of the seeding cloud. The larger the reflectivity factor of the lower layer of the seeding cloud is, the larger the velocity of cloud particles in the HD region, which conforms to the physical principle. As the height decreases to the base of the feeding cloud, the non-autocorrelation coefficient decreases from 0.4 to –0.2, indicating that the average terminal velocity of cloud particles in the HD region is only positively correlated with the reflectivity factor near the top of the feeding cloud, that is, cloud particles in the HD region only affect the clouds near the top of the feeding cloud, but have little effect on the lower part of the feeding cloud. This shows that the reflectivity factor in the middle and lower part of the feeding cloud has little correlation with the terminal velocity of cloud particles in the HD region.

In generally, the effect of seeding cloud on feeding cloud is mainly manifested in the middle and upper part of feeding cloud, that is, the seeding effect activing in the effective seeding depth. During the seeding period, the cloud particle size is small (low reflectivity factor) from the top of feeding cloud upward to the 1km height. From top to bottom in the ESD, the size of cloud particles increased (the reflectivity factor increased), indicating that seeding mainly occurred in this depth. After the end of seeding, the continuous influence of the seeding process in the feeding cloud can be understood as the delay of seeding benefits, and also can be understood as the seeding process inside the feeding cloud, that is, the seeding of the middle part of the feeding cloud to its lower part.

4. Statistical characteristics

To reveal the characteristics of the seeder-feeder phenomenon of bilayer cloud over the Shanxi-Guanzhong Plain, China, the observation results by MMCR from winter to the next spring from 2021 to 2022 were analyzed, because a large range of compact and stable stratiform clouds often appear in the region during this season. During the observation period, MMCR observed 11 cases of seeder-feeder process in stratiform clouds. Table 4 lists the time of seeder-feeder process, THSC, BHSC, THFC, HD, t1, t2, t3, the phase of feeding cloud base and precipitation state on the ground. According to the precipitation records observed by the surface rain gauge, Table 4 shows that there were 6 cases with precipitation occurrences (one with snowfall) after the seeder-feeder process occurred. In 4 cases, the base height of feeding clouds dropped to about 560m, and the radial velocity at the cloud base was measured to be –2 ~ –3ms^{-1}, these cloud particles were liquid, so it can be seen that there was virga (drizzle that did not fall to the ground) at the bottom of the feeding clouds. In the process of 31 March, 2022, the echo intensity of the middle and lower part of the feeding cloud increased after seeding, and the cloud particles mainly moved down. However, due to the high height of the cloud base (about 3.9 km), the retrieved phase showed mixed phase, and no precipitation was observed by the ground rain gauge.

Table 4 Lists of the characteristic parameters of the seeder-feeder phenomenon for 11 cases of bilayer stratiform cloud from 2021 to 2022.

Type	Time	THSC /(km)	BHSC /(km)	THFC /(km)	HD /(km)	t1 /(min)	t2 /(min)	t3 /(min)	phase of feeding cloud base	Precipitation state
I	2021-11-29	10.23	6.00	5.20	0.80	101.5	91.3	114.9	rain	Yes
	2022-02-06	8.20	5.10	4.30	0.80	40.2	98.2	44	ice	No
	2022-02-06	8.43	5.61	4.86	0.75	49.1	113.9	33.6	snow	Yes
	2022-04-30	9.21	5.80	4.84	0.96	73.6	65.1	34.1	rain (virga)	No
	2022-11-16	8.79	5.71	4.77	0.94	23.7	36.3	9.0	rain (virga)	No
II	2021-01-23	9.45	6.12	4.50	1.62	80.3	59.6	29.5	rain (virga)	No
	2021-03-10	11.04	7.21	6.06	1.15	67.9	138.0	45.3	rain	Yes
	2022-03-31	10.02	7.74	6.25	1.49	30.3	30.9	23.3	mixed phase	No
	2022-06-04	10.23	6.99	5.43	1.56	15. 7	41.7	13.4	rain	Yes
III	2022-04-24	10.62	9.26	8.15	1.11	30.0	103.1	41.8	rain	Yes
	2022-11-08	10.65	8.04	5.82	2.22	35.8	47.0	17.5	rain	Yes

Table 5 Statistical results of characteristic parameters of three types of the seeder-feeder phenomenon.

Type	Samples	Variable	THSC /(km)	BHSC /(km)	THFC /(km)	HD /(km)	t1 /(min)	t2 /(min)	t3 /(min)
I	5	Mean	8.97	5.64	4.79	0.85	58	81	47
		RMSE	0.51	0.09	0.08	0.01	741	747	1282
II	4	Mean	10.18	7.02	5.56	1.46	60	68	28
		RMSE	0.33	0.34	0.47	0.03	452	1756	134
III	2	Mean	10.64	8.65	6.99	1.67	33	75	30
		RMSE	0.00025	0.37	1.36	0.31	8	787	148

Based on the characteristic parameters of seeding cloud and feeding cloud listed in Table 4, the seeding process can be generally divided into three categories according to THSC and HD. The seeding process of type I has low seeding height ((BHSC<6 km) and small HD (HD⩽1km), the type II has higher seeding height (6km⩽BHSC＜8km) and larger HD (HD⩾1km), and the type III also has higher seeding height (BHSC⩾8 km,) and larger HD (HD⩾1km). The Table 5 shows the characteristic parameter distributions of these three types of seeder-feeder processes. The average thickness of HD in the type I is 0.85km, the average length of seeding time t2 is 81min, and the average duration of seeding effect time t3 is 47min (the longest among the three types of the seeder-feeder process). The average HD thickness of type III is the deepest (1.67 km), and the duration of seeding time t2 and seeding effect duration t3 are longer than those of type II.

In order to expose the internal mechanism of the seeder-feeder phenomenon, the distribution of probability density with height (DPDH) for the reflectivity factor, radial velocity, spectral width, particle terminal velocity and vertical velocity of air flow in these three seeder-feeder types were calculated and plotted. Figs 7a1, 7b1 and 7c1 show the differences in the distribution of reflectivity factor with height in the three types before seeding. The differences of HD and its height before seeding were clearly shown, and the reflectivity factor of feeding cloud before seeding was small. Figs 7a2, 7b2 and 7c2 clearly show that the reflectivity factor of both seeding and feeding clouds increase during the seeding period, especially the cloud base height of the feeding clouds decreases significantly, indicating that the development of feeding clouds caused by seeding is likely to cause precipitation. After seeding, the reflectivity factor of seeding clouds weakened and their thickness thinned (even disappeared in the type III), but the lower part of feeding clouds continued to develop (Figs 7a3, 7b3, 7c3), especially in the type I. The above shows that when the HD is small and its height is low (type I), the seeding cloud has the greatest influence on the feeding cloud, because in this case, the distance between the seeding cloud and the feeding cloud is short, and the seeders are easy to affect the feeding cloud.

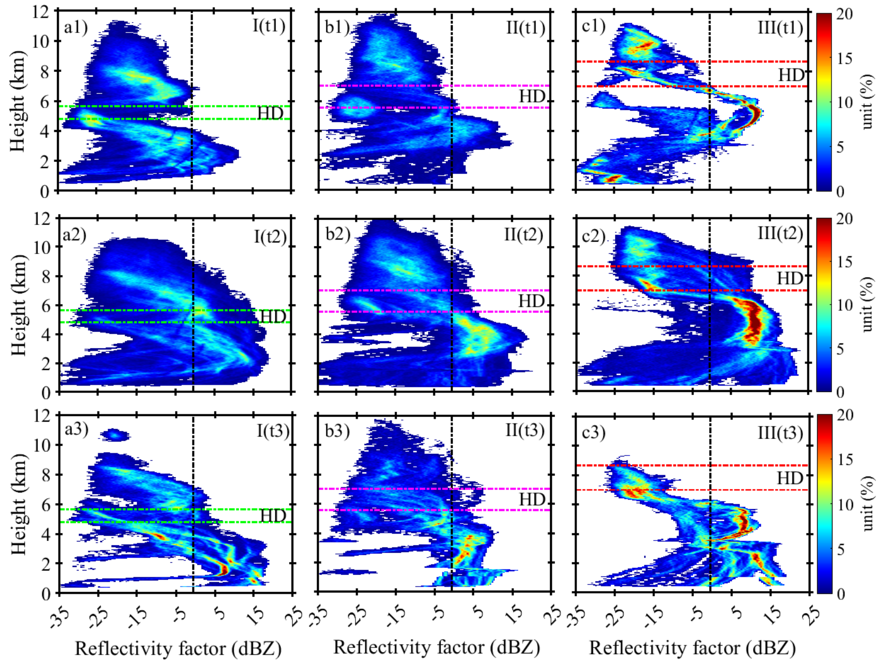

Figure 7 The DPDHs of reflectivity factor in three types of seeder-feeder process before (t1), during (t2) and after (t3) seeding. The type I (5 cases) on the left column, the type II (4 cases) in the middle column, and the type III (2 cases) in the right column. Note: the HD of type I is thin and low in height, the HD of type II is thick and slightly higher in height, and the HD of type III is thick and the highest in height, the same below.

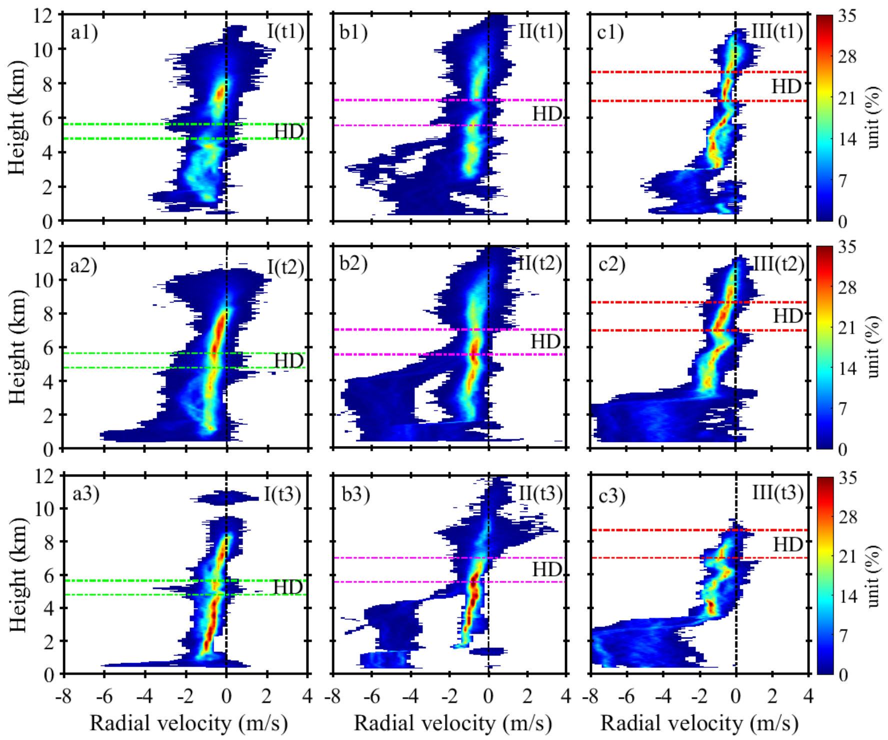

Figure 8 The DPDHs of radial velocity in three types of seeder-feeder process before (t1), during (t2) and after (t3) seeding.

The cloud particle radial velocity detected by MMCR is the actual motion velocity of cloud particles in the cloud, which can be understood as the synthesis velocity of the vertical air flow velocity and the terminal velocity of cloud particles. The DPDHs of radial velocity in three types are plotted in Fig. 8, which shows a weak rising movement in the upper part of the seeding cloud before seeding in three types, while a weak sinking movement appears in the lower part. In the feeding cloud, a weak subsidence exists consistently with slightly larger near the ground. In general, the radial velocity of most cloud particles in seeding cloud and feeding cloud keeps sinking motion, and the sinking motion increases with decreasing height. The radial velocity of cloud particles in seeding cloud and feeding cloud remained the same as before seeding. However, after seeding, the negative radial velocity of cloud particles decreased (subsidence motion increased) in the first type both seeding and feeding clouds, the same to the second and third types. In the meantime, seeding clouds disappeared in the third type (consistent with Fig. 7c3). The most important feature is that the radial velocity of cloud particles increases with the decrease of height from before seeding to seeding process and after seeding for the three types of seeder-feeder process. After seeding, the negative radial velocity of cloud particles in the lower part of the feeding cloud decreased significantly.

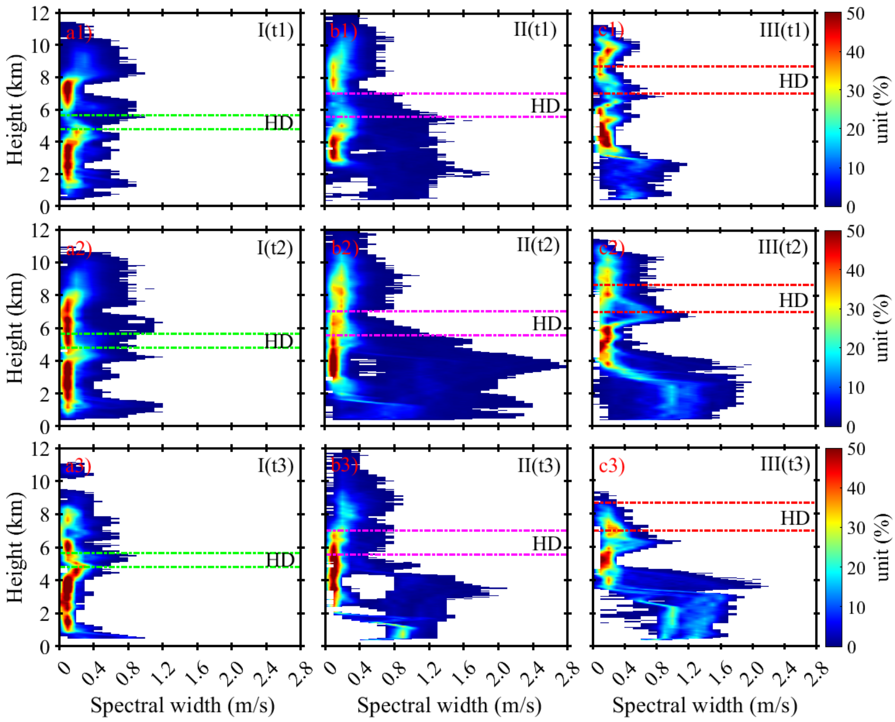

Figure 9 The DPDHs of spectral width in three types of seeder-feeder process before (t1), during (t2) and after (t3) seeding.

The velocity spectral width of cloud particle detected by MMCR reflects the range of cloud particle velocity. A larger value indicates a larger change in cloud particle velocity, while a smaller value indicates uniform cloud particle velocity. Fig. 9 shows the DPDHs of spectral width in three types of seeding and feeding clouds. The figure shows that the most velocity spectral width of the seeding and feeding clouds is less than 0.4 ms^{-1}, and the distribution of particle velocity spectral width in the type I is the narrowest (most of them are less than 0.2 ms^{-1}). Moreover, the velocity spectral width did not change significantly before and during seeding (Figs 9a1 and a2). But it became significantly narrower after seeding (Fig. 9a3), which indicates a relatively uniform of the velocity of cloud particles.

That was consistent with the DPDHs of the radial velocity with height as shown in Fig. 8 a3. The velocity spectral width distribution of the second and third types is wider than that of the type I. The maximum of the velocity spectral width reaches more than 1.6 ms^{-1}, and the velocity spectral width in feeding clouds is wider than that in seeding clouds, i.e. the velocity of cloud particles in feeding clouds is greatly different. In the process of seeding, the velocity spectral width of cloud particles for the type II and III became significantly wider (Figs. 9b2 and c2), which is evidence of the seeding effect resulting in a wide velocity distribution of cloud particles within the feeding cloud. After seeding, the velocity spectral width in feeding cloud of the both types still remained relatively wide (Figs. 9b3 and c3). In the HD area, the velocity spectrum width is wider in the type II and III than in the type I during seeding, which may portend a wider distribution of the cloud particle size in the second and the type III. While in the top of the feeding cloud, there is a small velocity spectrum width for the three types, which hints the relatively uniform of cloud particle velocity and the narrow distribution of cloud particle sizes.

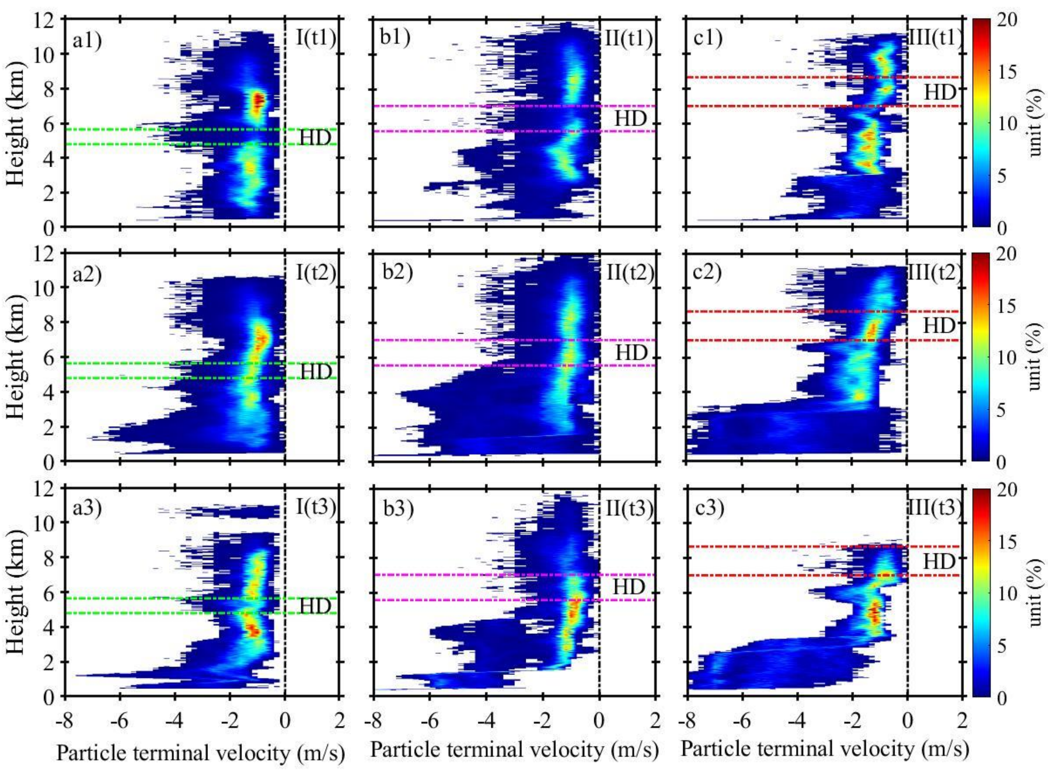

Figure 10 The DPDHs of the particle terminal velocity in three types of seeder-feeder process before (t1), during (t2) and after (t3) seeding.

The terminal velocity of cloud particles is the net velocity of cloud particles after deducting the air flow velocity from the radial velocity of cloud particles. As shown in Fig. 10, the DPDHs of the particle terminal velocity in the three types of seeding and feeding clouds varies. In general, the particle terminal velocity of the three types mainly ranges from –0.5 ms^{-1} to –2 ms^{-1}, and the distribution of the particle terminal velocity during the seeding process (t2) and after the seeding process (t3) is wider than that before the seeding (t1). In the seeding process, the terminal velocity distribution is the widest (the maximum reaching to –6 ms^{-1} in the type II, and to –8 ms^{-1} in the type III). The large terminal velocity of cloud particles is located at the lower part of the feeding cloud after the seeding for the three types, which is likely to be caused by the seeding effect to increase the size of cloud particles under feeding clouds. Then, under the action of gravity, the descending speed of cloud particles increases, and even rainfall occurs (the type III). During the seeding period of the three types (Fig. 10a2, b2, c2), the terminal velocity of cloud particles increased slightly with the descending height from the HD to the top of the feeding cloud, indicating that the size of seeders of the HD increased during the descending process and when they entered the upper part of the feeding cloud, which reflected the seeding effect of seeders. In the middle to lower part of the feeding cloud, the distribution of the terminal velocity is wide, which may be caused by the development of the feeding cloud itself. After end of the seeding in the three types (Figs. 10a3, b3, c3), the terminal velocity of cloud particles increases in the middle and lower part of the feeding cloud, which could be understood as the delay of seeding effect to the lower part of the feeding cloud during the seeding period.

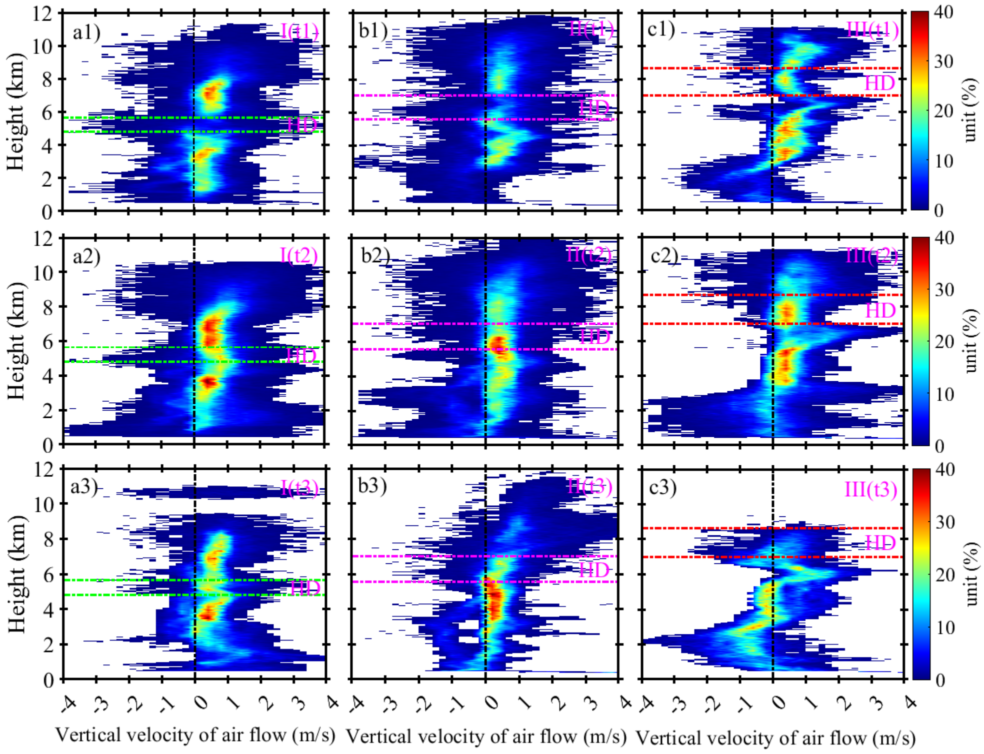

Figure 11 The DPDHs of the vertical velocity of air flow in three types of seeder-feeder process before (t1), during (t2) and after (t3) seeding.

The vertical velocity distribution of airflow in clouds is the reflection of the dynamic structure of clouds. The airflow in stratiform clouds is usually slow, and the size and concentration of cloud particles change little. Fig. 11 shows the DPDHs of the vertical velocity of airflow in the three types of seeding and feeding clouds. It shows that updraft and downdraft exist simultaneously in the cloud. The vertical velocity of airflow in the upper part of the seeding cloud is slightly larger than that in the lower part, which provides meteorological conditions for the growth of ice crystals in the seeding cloud. The updraft transport water vapor needed for the growth of ice particles, and also increases the probability of collision between particles. The updraft velocity at the top of the feeding cloud is also slightly greater than that at the base. There are the slight difference between the three types, among which the type I and II are dominated by weak updrafts before, during and after seeding, and HD region is also dominated by weak updrafts, the updrafts are mainly distributed in the range of 0 ~1 ms^{-1} (probability density is greater than 20%). The probability density of strong or weak updraft (greater than 1 ms^{-1} or less than 0 ms^{-1}) is less than 20%. For the type III, before and during seeding, the DPDHs with height for the vertical velocity of airflow was similar to that of the type I and II, but after seeding, the large downdraft appeared in the HD region and in the middle and lower part of the feeding cloud. Fig. 10c3 also showed that the cloud particles in the lower part of the feeding cloud mainly moved down, and the echo showed that precipitation appeared at the bottom of the feeding cloud.

To understand the relationship between cloud particle variation and echo signal, the correlation coefficient between cloud particle terminal velocity and corresponding reflectivity factor in each case of the three types during seeder-feeder period (t2) was calculated, and then averaged according to different categories. The height of average HD thickness in each type is taken as the basis, and the correlation coefficient profiles and average reflectivity factor profiles of the corresponding categories are obtained, as shown in Fig. 12. The cyan shaded area in the figure is the ESD layer. The average reflectivity factor profiles in the figure show that the height and thickness of the HD layer in the three types continuously increase from the type I to the type III, while the thickness of the ESD layer is on the contrary. The ESD in the type I is the thickest and it is the thinnest in the type III, which gives the conclusion that the HD height is high, and the ESD thickness is thin during seeding process. This process can be understood as that when HD is high, the cloud particles are small (that is, light particles in weight), so their falling speed is also small (see Fig. 10b2), so the depth of their falling into the top layer of the feeding cloud is also small. On the contrary, when the cloud particles in HD are larger (i.e. heavier), the height of HD will be lower, so these particles will enter deeper into the feeding cloud, such as the type I.

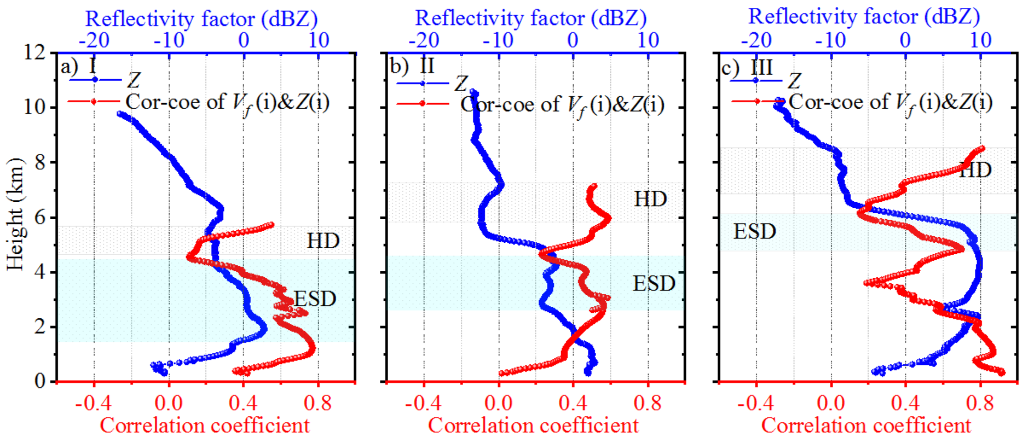

Figure 12 Autocorrelation coefficient profiles (red line) between cloud particle terminal velocity and reflectivity factor (blue line) during seeding (t2) for the type I (a), the type II (b) and the type III (c)

Fig. 12a shows more details in the feeding cloud such as the reflectivity factor increases with the decrease of the height and reaches the maximum value at 2 km, and the correlation coefficient also increases simultaneously with the reflectivity factor. That says close relationship between the reflectivity factor and the terminal velocity of cloud particles. The essence is that when the terminal velocity of cloud particles is large, it means that the cloud particles have a large mass and a large scale, then the reflectivity factor must be large. Fig. 10a2 also shows that there are the certain proportion of cloud particles in the middle and lower part of the ESD layer with the large sinking speed. However, at the base of feeding cloud, the reflectivity factor and the correlation coefficient decrease, indicating that there is basically no seeding effect at the base of feeding cloud during t2 period. The reflectivity factor increased rapidly but the correlation coefficient decreased rapidly at the top of feeding cloud in the second type. It is estimated that because the seeders in the HD region just fell into the top of the feeding cloud resulting in the number of cloud particles increased at the top, but these particles did not have time to grow, so although the echo reflectivity factor increased, the correlation coefficient decreased rapidly. When the seeders drop to a certain depth in the feeding cloud, the interaction between cloud particles such as collision occurs so that the correlation coefficient between cloud particle terminal velocity and echo reflectivity factor increases synchronously. Below the ESD region, the correlation coefficient decreases rapidly with the decrease of height, but the reflectivity factor continues to increase, which is probably caused by the high number of particles in the layer. In the third type, as the seeders enter the ESD region the reflectivity factor increases rapidly with the decrease of height together with the correlation coefficient increasing rapidly to the maximum. In the height from 5 km to 3.5 km, the correlation coefficient decreases obviously with the decrease of height, but the reflectivity factor maintains a large value (about 10 dBZ), which may indicate the high concentration of cloud particle in the height. In the lower part of the feeding cloud, the reflectivity factor decreases with the decrease of the height, while the correlation coefficient increases, indicating that the particle terminal velocity in this height also decreases. It is likely that the cloud particles are so small that some of them evaporate, causing both the reflectivity factor and the final particle velocity to decrease simultaneously. In general, the depth of seeders injecting the feeding cloud is limited, and the lower the height and thinner the thickness of HD, the lower the height and thicker the thickness of ESD.

5. Conclusions

In this paper, the data of bilayer cloud in winter to the next spring detected by MWCR are analyzed, and the seeder-feeder phenomenon between the bilayer clouds in Xi 'an area is found. By defining the key parameters of the seeding cloud and the feeding cloud, such as the HD between the bilayer cloud and the ESD of the feeding cloud, the calculation method of the parametric probability density distribution with height and the analysis method of the correlation coefficient profile between the cloud particle terminal velocity and the reflectivity factor are adopted. The results show that: (1) During the 11 cases of bilayer cloud seeding and feeding process, the seeding effect had the significant impact on the macro- and micro- parameters of the feeding cloud, which was mainly manifested in that the seeding effect caused the significant increase of the reflectivity factor and the terminal velocity of cloud particles in the feeding cloud. Therefore, it was speculated that the seeding effect caused the significant increase in the particle size of the feeding cloud. (2) According to the distribution characteristics of ESD thickness and height, the seeder-feeder process of bilayer cloud can be divided into three categories, the type I has thin HD layer with low height, and its ESD layer is thick; The type III has thick HD layer with high height, its ESD layer is thin; The values of both HD and ESD of the type II lie between the type I and III. It can be inferred that the lower the height and thinner the thickness of HD, the lower the height and thicker the thickness of ESD; the reverse is also true. (3) According to the analysis results of 11 cases, the seeder-feeder process and related parameter distribution of the bilayer stratiform cloud are shown in Fig. 13, that is, during the evolution of bilayer cloud, the phenomenon of cloud particles from the lower part of the upper-layer cloud seeding the lower-layer cloud will occur under appropriate weather background, that is, the distribution of air flow is unique with the height, and there is the relatively obvious updraft at the top of the seeding cloud. In the seeding layer (HD region and ESD region), the sinking motion of air flow and cloud particles is obvious, and when there is rainfall, the sinking motion at the base of the feeding cloud is stronger, and there is a small amount of down-flow region in the seeding cloud and the feeding cloud, but weak up-flow in the bilayer cloud. The seeding process can last up to 2 hours, but most seeding lasts for tens of minutes. Generally, seeding takes place at –25°C to –10°C within the cloud. The seeding effect plays actions on the precipitation (rain or snow) intensity in the feeding cloud will be shown in the results of subsequent studies.

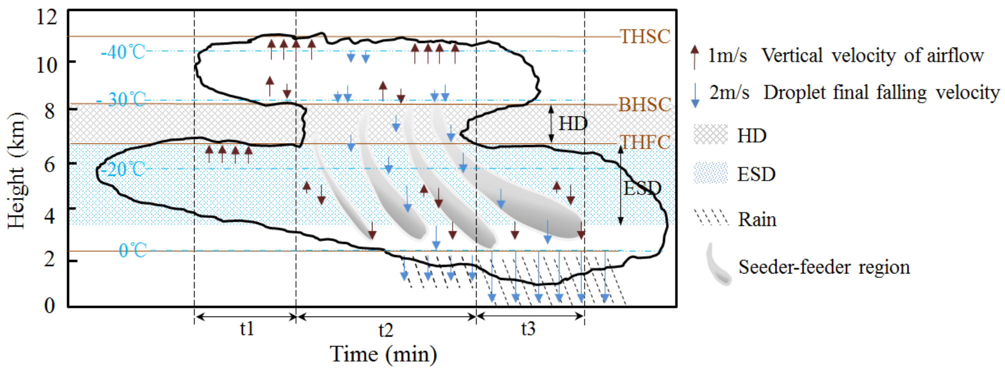

Figure 13 Schematic diagram of the natural seeder-feeder process and related parameter distribution.

Data availability

The data and codes related to this article are available upon request from the corresponding author.

Author contributions

Conceptualization: Huige Di
Investigation: Huige Di
Methodology: Huige Di
Software: Yun Yuan
Writing — original draft: Huige Di & Yun Yuan
Writing — review & editing: Huige Di
Supervision: Huige Di
Data collation: Yun Yuan

Competing interests

The authors declare that they have no conflicts of interest related to this work.

Acknowledgements

We express our gratitude to the Xi'an Meteorology Bureau of Shaanxi Province, Xi'an, Shehong Li, Shuicheng Bai, and Mei Cao for providing the relevant supporting data.

Financial support

This research was supported by the National Natural Science Foundation of China, the Innovative Research Group Project of the National Natural Science Foundation of China (Grant Nos. 42130612, 41627807), and the Ph.D. Innovation fund projects of Xi'an University of Technology (Fund No. 310-252072106).

References

1. Braham, R. R.: Cirrus Cloud Seeding as a Trigger for Storm Development, J. Atmos. Sci, 24, 311–312, https://doi.org/10.1175/1520-0469(1967)024<0311:CCSAAT>2.0.CO;2, 1967.
2. Cheng, C., and Yi, F.: Falling Mixed-Phase Ice Virga and their Liquid Parent Cloud Layers as Observed by Ground-Based Lidars, Remote Sens, 12, 2094, https://doi.org/10.3390/rs12132094, 2020.
3. Choularton, T.W., and Perry, S.J.: A model of the orographic enhancement of snowfall by the seeder-feeder mechanism, Quart. J. R. Met. Soc, 112, 335-345, https://doi.org/10.1002/qj.49711247204, 1986.
4. Di, H., Yuan, Y., Yan, Q., Xin, W., Li, S., Wang, J., Wang, Y., Zhang, L., and Hua, D.: Determination of atmospheric column condensate using active and passive remote sensing technology, Atmos. Meas. Tech, 15, 3555–3567, https://doi.org/10.5194/amt-

15-3555-2022, 2022.

5. Dong, X., Zhao, C., Huang, Z., Mai, R., Lv, F., Xue, X., Zhang, X., Hou, S., Yang, Y., Yang, Y., and Sun, Y.: Increase of precipitation by cloud seeding observed from a case study in November 2020 over Shijiazhuang, China, Atmos. Res, 262, 105766, https://doi.org/10.1016/j.atmosres.2021.105766, 2021.
6. Doviak, R. J., Zrnic, D. S., and Schotland, R. M.: Doppler radar and weather observations, Appl Optics, 33, 4531, 1994.
7. Fernández-González, S., Valero, F., Sánchez, J. L., Gascón, E., López, L., García-Ortega, E., and Merino, A.: Analysis of a seeder-feeder and freezing drizzle event, J. Geo-phys. Res. Atmos, 120, 3984–3999, https://doi.org/10.1002/2014jd022916, 2015.
8. French, J.R., Friedrich, K., Tessendorf, S.A., Rauber, R.M., Geerts, B., Rasmussen, R.M., Xue, L., Kunkel, M.L., and Blestrud, D.R.: Precipitation formation from orographic cloud seeding. P, Natl. Acad. Sci. Usa, 115, 1168–1173, https://doi.org/10.1073/pnas.1716995115, 2018.
9. Geerts, B., Pokharel, B., and Kristovich, D.A.R.: Blowing Snow as a Natural Glaciogenic Cloud Seeding Mechanism, Mon. Weather. Rev, 143, 5017–5033, https://doi.org/10.1175/MWR-D-15-0241.1, 2015.
10. Görsdorf, U., Lehmann, V., Bauer-Pfundstein, M., Peters, G., Vavriv, D., Vinogradov, V., and Volkov, V.: A 35-GHz Polarimetric Doppler Radar for Long-Term Observations of Cloud Parameters—Description of System and Data Processing, J. Atmos. Ocean. Technol, 32, 675–690, https://doi.org/10.1175/jtech-d-14-00066.1, 2015.
11. Hall, W.D., and Pruppacher, H.R.: The Survival of Ice Particles Falling from Cirrus Clouds in Subsaturated Air, J. Atmos. Sci, 33, 1995–2006, https://doi.org/10.1175/1520-0469(1976)033<1995:tsoipf>2.0.co;2, 1976.
12. He, Y., Liu, F., Yin, Z., Zhang, Y., Zhan, Y., and Yi, F.: Horizontally oriented ice crystals observed by the synergy of zenith- and slant-pointed polarization lidar over Wuhan (30.5°N, 114.4°E), China, J. Quant. Spectrosc. Ra, 268, 107626, https://doi.org/10.1016/j.jqsrt.2021.107626, 2021.
13. He, Y., Yi, F., Liu, F., Yin, Z., Yi, Y., Zhou, J., Yu, C., and Zhang, Y.: Natural seeder-feeder process originating from mixed-phase clouds observed with polarization lidar and radiosonde at a mid-latitude plain site, J. Geo-phys. Res. Atmos, 127, e2021JD036094, https://doi.org/10.1029/2021JD036094, 2022.
14. Heymsfield, A.J., Schmitt, C., Bansemer, A.: Ice Cloud Particle Size Distributions and Pressure-Dependent Terminal Velocities from In Situ Observations at Temperatures from 0° to −86°C, J. Atmos. Sci, 70, 4123–4154, https://doi.org/10.1175/jas-d-12-0124.1, 2013.
15. Hill, F. F., Browning, K. A., and Bader, M. J.: Radar and Raingauge Observations of Orographic Rain over South Wales, Q. J. Roy. Meteor. Soc, 107, 643–670, https://doi.org/10.1002/qj.49710745312, 2007.
16. Hong, Y.: Research Progress of Stratiform Cloud Structure and Precipitation Mechanism and Discussion on Artificial Precipitation Problems, Clim. Environ. Res, 17, 937-950, https://doi.org/10.3878/j.issn.1006-9585.2012.06.31, 2012.
17. Hou, T., Lei, H., and Hu, Z.: A comparative study of the microstructure and precipitation mechanisms for two stratiform clouds in China, Atmospheric Research, 96, 447–460, https://doi.org/10.1016/j.atmosres.2010.02.004, 2010.
18. Houghton, H. G.: On the Physics of Clouds and Precipitation, in: Compendium of Meteorology: Prepared under the Direction of the Committee on the Compendium of Meteorology, edited by: Byers, H. R., Landsberg, H. E., Wexler, H., Haurwitz, B., Spilhaus, A. F., Willett, H. C., Houghton, H. G., and Malone, T. F., American Meteorological Society, Boston, MA, 165–181, https://doi.org/10.1007/978-1-940033-70-9_14, 1951.
19. Kollias, P., Albrecht, B. A., Lhermitte, R., and Savtchenko, A.: Radar observations of updrafts, downdrafts, and turbulence in fair-weather cumuli, J. Atmos. Sci, 58, 1750-1766, https://doi.org/10.1175/1520-0469(2001)058%3C1750:ROOUDA%3E2.0.CO;2, 2001.
20. Kollias, P., Albrecht, B.A., Marks, F.: Why Mie? Accurate observations of vertical air velocities and raindrops using a cloud radar, Bull. Amer. Meteor. Soc, 83, 1471–1483, https://doi.org/10.1175/bams-83-10-1471, 2002.
21. Kollias, P., Rémillard, J., Luke, E., Szyrmer, W.: Cloud radar Doppler spectra in drizzling stratiform clouds: 1. Forward modeling and remote sensing applications, J. Geophys. Res, 116, D13201, https://doi.org/10.1029/2010JD015237, 2011.
22. Korolev, A. and Isaac, G.: Phase transformation of mixed-phase clouds, Q J Roy Meteor Soc, 129, 19–38,

https://doi.org/10.1256/qj.01.203, 2003.

23. Korolev, A. V., Isaac, G. A., and Hallett, J.: Ice particle habits in Arctic clouds, Geophysical Research Letters, 26, 1299–1302, https://doi.org/10.1029/1999GL900232, 1999.

24. Korolev, A. V., Isaac, G. A., Cober, S. G., Strapp, J. W., and Hallett, J.: Microphysical characterization of mixed-phase clouds, Q J Roy Meteor Soc, 129, 39–65, https://doi.org/10.1256/qj.01.204, 2003.

25. Liu, L., Ding, H., Dong, X., Cao, J., and Su, T.: Applications of QC and Merged Doppler Spectral Density Data from Ka-Band Cloud Radar to Microphysics Retrieval and Comparison with Airplane in Situ Observation, Remote. Sens, 11, 1595, https://doi.org/10.3390/rs11131595, 2019.

26. Locatelli, J. D., Hobbs, P. V., and Biswas, K. R.: Precipitation from Stratocumulus Clouds Affected by Fallstreaks and Artificial Seeding, J. Clim. Appl. Meteorol., 22, 1393–1403, https://doi.org/10.1175/1520-0450(1983)022<1393:PFSCAB>2.0.CO;2, 1983.

27. Lowenthal, D.H., Hallar, A.G., David, R.O., Mccubbin, I.B., and Mace, G.G.: Mixed Phase Orographic Cloud Microphysics during StormVEx and IFRACS, Atmos. Chem. Phys, 19, 5387–5401, https://doi.org/10.5194/acp-19-5387-2019, 2019.

28. Luke, E. P., and Kollias, P.: Separating Cloud and Drizzle Radar Moments during Precipitation Onset Using Doppler Spectra, J. Atmos. Ocean. Technol, 30, 1656–1671, https://doi.org/10.1175/jtech-d-11-00195.1, 2013.

29. Myagkov, A., Seifert, P., Wandinger, U., Bühl, Johannes., Engelmann, R.: Relationship between temperature and apparent shape of pristine ice crystalsderived from polarimetric cloud radar observations during the accept campaign, Atmos. Meas. Tech, 9, 3739-3754, https://doi.org/10.5194/amt-9-3739-2016, 2016.

30. Proske, U., Bessenbacher, V., Dedekind, Z., Lohmann, U., and Neubauer, D.: How frequent is natural cloud seeding from ice cloud layers (< −35◦C) over Switzerland?, Atmos. Chem. Phys, 21, 5195–5216, https://doi.org/10.5194/acp-21-5195-2021, 2021.

31. Purdy, J. C., Austin, G. L., Seed, A. W., and Cluckie, I. D.: Radar evidence of orographic enhancement due to the seeder feeder mechanism, Meteorol. Appl, 12, 199–206, https://doi.org/10.1017/S1350482705001672, 2005.

32. Ramelli, F., Henneberger, J., David, R. O., Bühl, J., Radenz, M., Seifert, P., Wieder, J., Lauber, A., Pasqier, J. T., Engelmann, R., Mignani, C., Hervo, M., and Lohmann, U.: Microphysical investigation of the seeder and feeder region of an Alpine mixed-phase cloud, Atmos. Chem. Phys, 21, 6681-6706, https://doi.org/10.5194/acp-2020-772, 2021.

33. Ramelli, F., Henneberger, J., David, R.O., Lauber, A., Pasquier, J.T., Wieder, J., Bühl, J., Seifert, P., Engelmann, R., Hervo, M., and Lohmann, U.: Influence of low-level blocking and turbulence on the microphysics of a mixed-phase cloud in an inner-Alpine valley, Atmos. Chem. Phys, 21, 5151–5172, https://doi.org/10.5194/acp-21-5151-2021, 2021.

34. Robichaud, A. J., and Austin, G. L.: On the Modelling of Warm Orographic Rain by the Seeder-Feeder Mechanism, Q. J. Roy. Meteor. Soc, 114, 967–988, https://doi.org/10.1002/qj.49711448207, 1988.

35. Seifert, P., Ansmann, A., Mattis, I., Althausen, D., Tesche, M., Wandinger, Ulla., Muller, D., and Pérez, C.: Lidar-based profiling of the tropospheric cloud-ice distribution to study the seeder-feeder mechanism and the role of Saharan dust as ice nuclei, In: Proceedings of the 8th International Symposium on Tropospheric Profiling, Bergen, Norway, 2014.

36. Shupe, M. D., Kollias, P., Persson, P. O. G., and McFarquhar, G. M.: Vertical motions in Arctic mixed-phase stratiform clouds, J. Atmos. Sci, 65, 1304-1322, https://doi.org/10.1175/2007JAS2479.1, 2008.

37. Shupe, M. D., Uttal, T., and Matrosov, S. Y.: Arctic Cloud Microphysics Retrievals from Surface-Based Remote Sensors at SHEBA, J. Appl. Meteorol, 44, 1544–1562, https://doi.org/10.1175/jam2297.1, 2005.

38. Shupe, M. D.: A ground-based multisensory cloud phase classifier, Geophys. Res. Lett. 34, L22809, https://doi:10.1029/2007GL031008, 2007.

39. Tao, R., Zhao, K., Huang, H., Wen, L., Chen, H.: Snow Particle Size Distribution From a 2-D Video Disdrometer and Radar Snowfall Estimation in East China. IEEE Transactions on Geoscience and Remote sensing. 59, 196-207, http://doi.org/ 10.1109/TGRS.2020.2990920, 2020.

40. Vassel, M., Ickes, L., Maturilli, M., and Hoose, C.: Classification of Arctic multilayer clouds using radiosonde and radar data in Svalbard, Atmos. Chem. Phys, 19, 5111–5126, https://doi.org/10.5194/acp-19-5111-2019, 2019.

41. Wang, H., Zhang, H., Wang, W., Wang, J., Li, Y., and Wang, S.: Microphysical characteristics of precipitation in multi-source

mixed clouds, DQKX, 46, 886–902, https://doi.org/10.3878/j.issn.1006-9895.2107.21043, 2022.

42. Wang, Y., Kong, R., Cai, M., Zhou, Y., Song, C., Liu, S., Li, Q., Chen, H., and Zhao, C.: High small ice concentration in stratiform clouds over Eastern China based on aircraft observations: Habit properties and potential roles of secondary ice production, Atmos Res, 281, 106495, https://doi.org/10.1016/j.atmosres.2022.106495, 2023.
43. Wei, T., Xia, H., Hu, J., Wang, C., Shangguan, M., Wang, L., Jia, M., and Dou, X.: Simultaneous wind and rainfall detection by power spectrum analysis using a VAD scanning coherent Doppler lidar, Opt Express, 27, 31235, https://doi.org/10.1364/OE.27.031235, 2019.
44. Yan-Chao, H. and Fei-Fei, Z.: A Numerical Simulation Study of Precipitation Formation Mechanism of "Seeder-feeder" Cloud System, dqkx, 29, 885–896, https://doi.org/10.3878/j.issn.1006-9895.2005.06.05, 2005.
45. Yan-Chao, H. and Fei-Fei, Z.: The Study of Evaluation of Potential of Artificial Precipitation Enhancement in Stratiform Cloud System, dqkx, 30, 913–926, https://doi.org/10.3878/j.issn.1006-9895.2006.05.20, 2006.
46. Yu, G., Verlinde, J., Clothiaux, E. E., and Chen, Y.-S.: Mixed-phase cloud phase partitioning using millimeter wavelength cloud radar Doppler velocity spectra, J. Geophys. Res. Atmos., 119, 7556–7576, https://doi.org/10.1002/2013JD021182, 2014.
47. Yuan, Y., Di, H., Liu, Y., Cheng, D., Chen, N., Yan, Q., and Hua, D.: Confidence and Error Analyses of the Radiosonde and Ka-Wavelength Cloud Radar for Detecting the Cloud Vertical Structure, Remote. Sens, 14, 4462, https://doi.org/10.3390/rs14184462, 2022.
48. Yuan, Y., Di, H., Liu, Y., Yang, T., Li, Q., Yan, Q., Xin, W., Li, S., and Hua, D.: Detection and analysis of cloud boundary in Xi'an, China, employing 35 GHz cloud radar aided by 1064 nm lidar, Atmos. Meas. Tech, 15, 4989-5006, https://doi.org/10.5194/amt-15-4989-2022, 2022.
49. Yuan, Y., Di, H., Wang, K., Bai, S., Yan, Q., Cao, M., Zhang, Y., Wang, Y., and Hua, D.: Fine recognition technology of cloud phase based on multidimensional data, Acta Opt. Sin, 42, 268-278, https://doi.org/10.3788/AOS202242.1228002, 2022.